

Toward Tissue Penetration by MRI-powered Millirobots Using a Self-Assembled Gauss Gun

Aaron T. Becker, *Member, IEEE*, Ouajdi Felfoul, and Pierre E. Dupont, *Fellow, IEEE*

Abstract—MRI-based navigation and propulsion of millirobots is a new and promising approach for minimally invasive therapies. The strong central field inside the scanner, however, precludes torque-based control. Consequently, prior propulsion techniques have been limited to gradient-based pulling through fluid-filled body lumens. This paper introduces a technique for generating large impulsive forces that can be used to penetrate tissue. The approach is based on navigating multiple robots to a desired location and using self-assembly to trigger the conversion of magnetic potential energy into sufficient kinetic energy to achieve penetration. The approach is illustrated through analytical modeling and experiments in a clinical MRI scanner.

I. INTRODUCTION

Millimeter-scale robots have the potential to provide highly localized therapies with minimal trauma by navigating through the natural fluid-filled passageways of the body. While navigation through, e.g., the circulatory system or cerebrospinal fluid spaces, is sufficient for some applications, it can also be necessary to penetrate into the surrounding tissue. Examples include puncturing a membrane to release trapped fluid, opening a blocked passageway or delivering a drug to a tissue location several centimeters from a fluid-filled space. The forces required for tissue penetration, however, are substantially higher than those needed to propel a millirobot through a bodily fluid and, consequently, can be difficult to achieve. Prior tetherless systems for moving through tissue have relied on magnetic forces and torques produced by large external magnets to either pull magnetic spheres through brain tissue [1] or to rotate threaded magnetic cylinders through muscle tissue [2].

Alternatively, methods for tetherless robot propulsion and control have been developed that employ the magnetic gradients of clinical MRI scanners [3]–[6]. MRI also provides the capability to image both the robot and surrounding tissue to guide navigation. MRI-based millirobot navigation in the vasculature was first demonstrated in [3]. Recently, algorithms enabling the simultaneous MRI-based control of multiple millirobots [4], [7] and macro-scale rotary actuators [5], [6] have also been developed.

To date, however, the motion of MRI-powered millirobots has been constrained to fluid-filled spaces since the magnetic

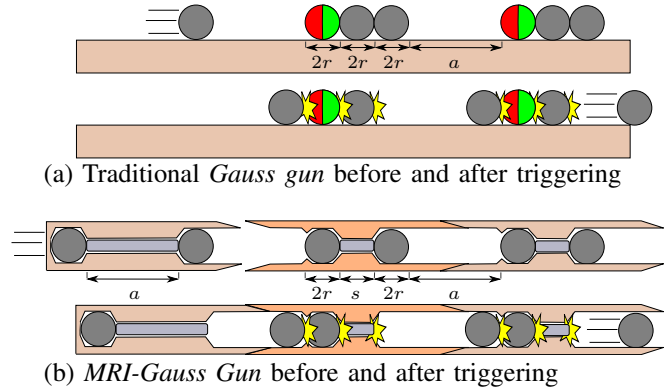


Fig. 1. Operation of a Gauss gun. (a) Standard design for use outside an MRI scanner shown before and after triggering. Magnetized spheres are red and green. Non-magnetized spheres are gray. (b) Design for use inside an MRI scanner shown before and after triggering. All spheres are magnetized when inside scanner. See video at <http://youtu.be/uJ4rFA8x2Js>.

gradients produced by the scanner are relatively weak. The maximum gradient produced by most clinical scanners is in the range of 20–40mT/m producing a force on a magnetized steel particle equal to 36–71% of its gravitational force. While it is possible to install custom high-strength gradient coils, such as the 400mT/m coil reported in [8], this approach is costly and can reduce the size of the MRI bore. While to facilitate motion within a fluid, a millirobot can be designed to be neutrally buoyant, the force magnitude produced by the magnetic gradient is not capable of producing tissue penetration.

Consider, for example, that a standard 18 gauge needle requires 0.59 ± 0.11 N of force to penetrate 10mm into muscle tissue [9]. Bioinspired design can somewhat reduce these forces, e.g., the backward-tipped barbs of the North American porcupine quill exhibit forces of 0.33 ± 0.08 N for 10mm of muscle penetration [9]. Nevertheless, to reproduce even these forces using an MRI with a steel needle would require a 3.3m long shaft – longer than the bore of the scanner. While the size of macro-scale MRI-based actuators permits the use of gear transmissions to trade off velocity and force [4], [10], this approach is not feasible at the millimeter scale. Therefore, to address the challenge of MRI-based tissue penetration, an alternative to gradient-based force production is needed.

The observation that tissue puncture force is inversely related to penetration velocity [11] motivates the concept of using energy storage and sudden release to perform penetration. Furthermore, while the maximum gradient forces produced

A. T. Becker is with the Dept. of Electrical and Computer Engineering, University of Houston, Houston, TX 77004, USA atbecker@uh.edu, O. Felfoul, and P. E. Dupont are with the Department of Cardiovascular Surgery, Boston Children's Hospital and Harvard Medical School, Boston, MA, 02115 USA first.name.lastname@childrens.harvard.edu. This work was supported by the National Science Foundation under IIS-1208509 and by the Wyss Institute for Biologically Inspired Engineering.

on a steel particle are low, the magnetic attraction forces between particles inside the scanner is, by comparison, quite high. Thus, the approach proposed here involves navigating individual millirobots to a target location and allowing them to self-assemble in a manner that focuses the stored magnetic potential energy as kinetic energy for tissue penetration.

The concept, illustrated in Fig. 1, corresponds to a Gauss gun or accelerator [12], [13]. Comprised of one or more stages, each stage is composed of a strong magnet, followed by two or more steel spheres (bearing balls). By colliding a single steel sphere with the first magnet, a chain reaction is initiated, greatly amplifying the speed of the first sphere.

In an MRI scanner, there is no need for permanent magnets, since steel is highly magnetized by the 3T magnetic field of an MRI. Each stage, containing two magnetized spheres separated by a nonmagnetic spacer, is individually stable. Using existing control approaches [4], [7], they can be navigated through fluid-filled spaces and self-assembled at a desired penetration location. The assembly can then be fired by a special trigger module consisting of two spheres separated by a spacer longer than that used in the individual stages. After firing, the assembly can be navigated out of the body.

The remainder of the paper is arranged as follows. The mathematical model of the MRI Gauss gun is derived in the next section. Section III details the design of experimental prototypes. Experiments evaluating self-assembly and penetration are provided in Section IV. Conclusions appear in Section V.

II. THEORY

Ferrous material placed inside the strong B_0 field of an MRI become strong magnets. This section describes the forces and torques these magnets exert on other magnets, the magnetic potential energy between these magnets, and how this energy is exploited in a Gauss gun.

A. Magnet Interaction Forces

Any ferrous material placed in the magnetic field of an MR scanner becomes a strong magnetic dipole. The gradient fields can then apply forces on these dipoles. Additionally, the dipoles exert forces on each other. Dipole forces overpower MRI gradient forces if the materials are closer than a threshold distance.

The magnetic field at position \mathbf{p}_2 generated by a spherical magnet at position \mathbf{p}_1 with magnetization \mathbf{m}_1 is [14]

$$\mathbf{B}_{\mathbf{p}_1}(\mathbf{p}_2) = \frac{\mu_0}{4\pi} \frac{3\mathbf{n}_{12}(\mathbf{n}_{12} \cdot \mathbf{m}_1) - \mathbf{m}_1}{|\mathbf{p}_2 - \mathbf{p}_1|^3}, \quad (1)$$

with $\mathbf{n}_{12} = (\mathbf{p}_2 - \mathbf{p}_1)/|\mathbf{p}_2 - \mathbf{p}_1|$. This is the *magnetic field of a dipole*. The force applied to a dipole at \mathbf{p}_1 with magnetic moment \mathbf{m}_1 by another dipole at \mathbf{p}_2 with magnetic moment \mathbf{m}_2 is approximated by

$$\mathbf{F}_{12} \approx \frac{3\mu_0}{4\pi} \frac{1}{|\mathbf{p}_2 - \mathbf{p}_1|^4} \left[5\mathbf{n}_{12} \left((\mathbf{m}_1 \cdot \mathbf{n}_{12}) (\mathbf{m}_2 \cdot \mathbf{n}_{12}) \right) - \mathbf{n}_{12} (\mathbf{m}_2 \cdot \mathbf{m}_1) - \mathbf{m}_1 (\mathbf{m}_2 \cdot \mathbf{n}_{12}) - \mathbf{m}_2 (\mathbf{m}_1 \cdot \mathbf{n}_{12}) \right]. \quad (2)$$

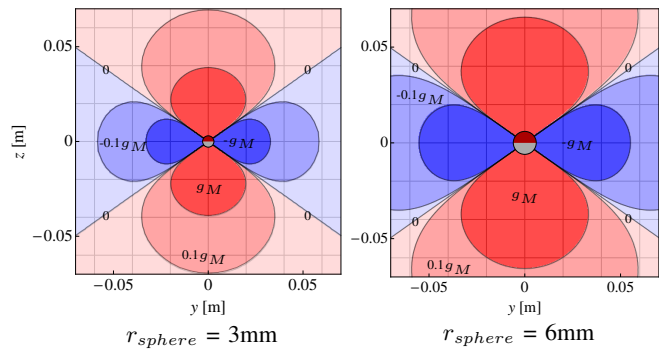


Fig. 2. Contour lines show the force component radially outward from a sphere at (0, 0) on an identical sphere in an MRI. The magnetic field is symmetric about the z -axis.

The torque applied on a dipole at \mathbf{p}_2 by a dipole at \mathbf{p}_1 is

$$\emptyset_{12} = \mathbf{m}_2 \times \mathbf{B}_{\mathbf{p}_1}(\mathbf{p}_2) \quad (3)$$

Inside a 3T MRI, a steel sphere becomes fully magnetized with magnetic saturation $M_s=1.36 \times 10^6$. The magnetic moment of a sphere with radius r_{sphere} is aligned with the MRI B_0 field:

$$\mathbf{m}(r_{sphere}) = \begin{bmatrix} 0 \\ 0 \\ 1 \end{bmatrix} \frac{4}{3} \pi r_{sphere}^3 M_s. \quad (4)$$

Figure 2 shows contour plots for the magnetic force exerted by two identical spheres on each other. The contour lines show $\mathbf{F} \cdot \mathbf{n}_{12}$, the force component radially outward from the sphere at $(0,0)$ compared to the maximum force provided by the gradient coils g_M . This force is attractive (red) along the z -axis and repulsive (blue) perpendicular to z . The magnetic field is symmetric about the z -axis. If two spheres move within the dark red region, they cannot be separated using the gradient field. The contour lines are drawn at $\mathbf{F}_{12} \cdot \mathbf{n}_{12} = g_M \cdot \{-1, -\frac{1}{10}, 0, \frac{1}{10}, 1\}$. The maximum force is along the z -axis

$$F_{\text{attraction}} = -\frac{8M_s^2\mu_0\pi r_1^3r_2^3}{3d^4}, \quad (5)$$

where d is the distance separating two spheres of radii r_1 and r_2 , each with magnetic saturation M_s . The vacuum permeability μ_0 is, by definition, $4\pi \times 10^{-7}$ V·s/(A·m).

The critical distance when the attractive force becomes greater than the maximum gradient force is $\sqrt[4]{\frac{2M_s\mu_0r_{sphere}^3}{gM}}$.

B. Magnetic Potential Energy

A Gauss gun converts the potential energy stored by an arrangement of magnets into kinetic energy.

The potential energy of two spherical magnets with magnetism M_s and radii r_1 and r_2 is

$$\begin{aligned} PE(d, r_1, r_2, M_s) &= -\frac{8M_s^2\mu_0\pi r_1^3r_2^3}{3}\int_d^\infty\frac{1}{x^4}\mathrm{d}x \\ &= -\frac{8M_s^2\mu_0\pi r_1^3r_2^3}{9d^3} = \frac{C_{r_1r_2}}{d^3} \end{aligned} \quad (6)$$

The constant $C_{r_1 r_2}$ includes all terms except the distance between the spheres. The change in potential energy, ΔPE , when moving from separation d_1 to separation d_2 is

$$\Delta PE(d_1, d_2) = C_{r_1 r_2} \left(\frac{1}{d_2^3} - \frac{1}{d_1^3} \right) \quad (7)$$

C. Gauss Gun Energy

When a Gauss gun is fired, at each stage at most one sphere is moving. The energy released at each stage is the summation of potential energy before and after the movement as sphere i moves from position p_i^- to position p_i^+ , as shown in the two-stage version in Fig. 1.

$$\begin{aligned} PE_i^- &= \sum_{i \neq j} C_{r_i r_j} \left(\frac{1}{(p_i^- - p_j)^3} \right) \\ PE_i^+ &= \sum_{i \neq j} C_{r_i r_j} \left(\frac{1}{(p_i^+ - p_j)^3} \right) \\ \Delta PE_i &= PE_i^+ - PE_i^- \end{aligned} \quad (8)$$

The total energy delivered by the Gauss gun is a sum of ΔPE_i , (8), calculated for each stage. This simplified analysis ignores mechanical energy losses, which include friction, inelastic collisions, and ohmic heating.

If the initial ball begins with zero velocity, the final velocity of the last steel sphere with mass m can be calculated according to the law of conservation of energy:

$$v = \sqrt{\frac{2\Delta PE}{m}}. \quad (9)$$

Interestingly, both the energy ΔPE and mass m scale with the cube of ball radius, and so cancel each other. This means that two Gauss guns that are identical up to a scaling factor will have the same final projectile velocity.

D. Self-Assembly Forces and Torques

The components of the Gauss gun are attracted to each other. Additionally, the strong B_0 field of the MRI produces a strong torque that aligns the components. These attraction forces, combined with the aligning torque, enable rapid self-assembly of the modules.

a) Component forces before and after firing: Consider two barrel components, each with two steel spheres of radius r and a separator of length s . If the components have an air gap a , where both s and a are in units of sphere radius r , the ratio of force between components before and after firing is

$$\left| \frac{\mathbf{F}_{12}^-}{\mathbf{F}_{12}^+} \right| = \frac{(2+a+s)^{-4} + (4+a+s)^{-4}}{(2+a)^{-4} + 2(4+a+s)^{-4} + (6+a+2s)^{-4}} \quad (10)$$

notice that r values cancel out. For $s < 4r$, the attraction force after firing is between 16% and 94% of the force before firing. This relationship is plotted in Fig. 3. Because the attraction force is always less after firing, it is possible to find r, a, s values such that the MRI gradient fields can separate components after firing.

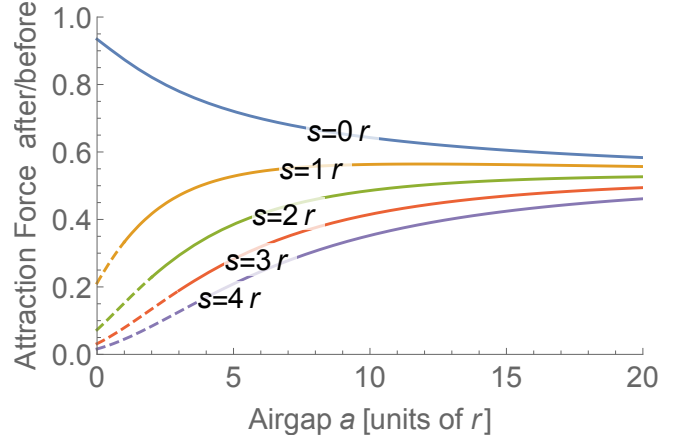


Fig. 3. Ratio of $\frac{\text{attraction force before firing}}{\text{attraction force after firing}}$ between two components.

b) Torque on a Gauss gun component: Because each Gauss gun component has at least two ferrous spheres, the MRI B_0 field creates a torque that acts to line the components parallel to the z -axis. Applying (3), with magnetic moments given by (4), on a component with sphere radii r_1 and r_2 , separated by s , and the line between the spheres at an angle of θ from z , generates the restoring torque

$$\tau = \frac{4}{3s^3} M_s^2 \pi \mu_0 r_1^3 r_2^3 \sin(2\theta) \quad (11)$$

Both decreasing s and increasing r_1 and/or r_2 increases this torque. This torque results in stable equilibrium configurations pointing along the $\pm z$ -axis and unstable equilibriums perpendicular to the axis. The stable equilibriums correspond with maximum attractive force between the spheres, and the unstable equilibriums with maximum repulsive force. The average torque on the spheres is $4/\pi$ the average force between the spheres.

III. DESIGN

There are four parameters that can be optimized in the design shown in Fig. 1: the sphere radius r , the intra-stage separation s , the inter-stage air gap a , and the number of stages N .

Each component contains two spheres and a separator. Each *barrel* contains a separator of length s and $1/2a$ of material to create an air gap at each end, with a total length of $4r + a + s$. The *trigger* component must have a separator at least as long as a to ensure automatic firing when the *trigger* is attached to another component. The *trigger* also contains connective material to create the air gap $a/2$, giving a total length of $1.5a + 4r$.

Tradeoffs between the parameters are shown in Fig. 4. Potential energy increases with the cube of ball radius, linearly with number of stages, and asymptotically increases to a limit with inter- and intra-component spacing.

A. Construction

Gauss guns are often composed of one or more neodymium magnets and several similarly sized steel

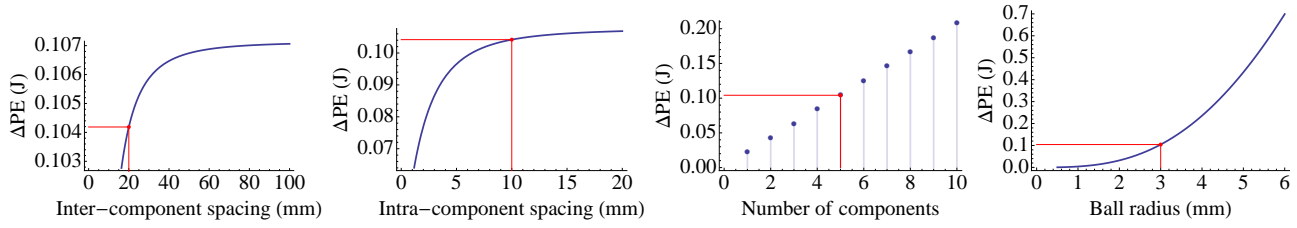


Fig. 4. Potential energy as a function of four design parameters. See design software at <http://demonstrations.wolfram.com/OptimizingAGaussGun/> [15].

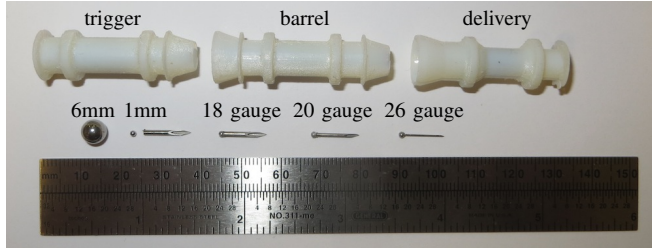


Fig. 5. Gauss gun components.

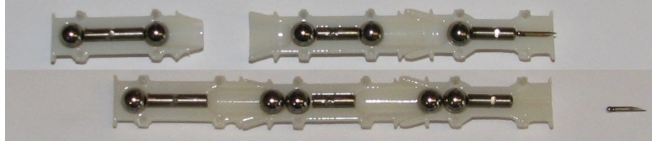


Fig. 6. Cross-section, three component Gauss gun before and after firing.

spheres. The Gauss guns described in this paper use chrome steel spheres (E52100 Alloy, McMaster 9292K41) for the magnets and shaped rods of nonmagnetic metal for spacers. This provides several benefits:

- inside an MRI, steel is a stronger magnet than neodymium
- spacer length is arbitrary and can be chosen to maximize energy
- leaving multiple magnets in tissue is potentially dangerous, leading, e.g., to bowel necrosis, perforation, volvulus, sepsis, and possible death [16], [17]. In contrast, the steel bearing balls used in this study lose their magnetism when removed from the magnetic field of the MRI
- MRI enables imaging and control to assemble components at target
- MRI enables controlled removal of components

The prototype Gauss gun components are shown in Fig. 5. The *barrel* components can be stacked to achieve stronger forces. A *trigger* component fires the Gauss gun. An optional *delivery* component can be used to administer the desired treatment, either a puncture or a drug delivery. Several projectiles were tested; a 6mm diameter sphere, a 1mm diameter sphere, an 18 gauge needle tip, and 1mm spheres connected to 18, 20, and 26 gauge needle tips. The steel spheres are TIG welded to the needle tips.

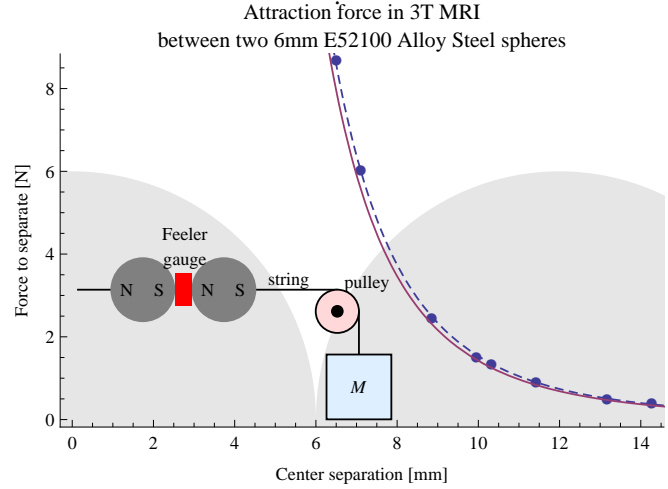


Fig. 7. The force between two magnetized spheres was determined by placing plastic feeler gauges between them and increasing mass M until the spheres separated. The experimental force (dashed) is plotted next to the theoretical value.

B. Material Selection

The attraction force between two spherical magnets is given by (5). This can be verified by measuring the force required to break the magnetic bond at different initial separation distances: secure string to two magnets, place different nonmagnetic feeler gauges (McMaster-Carr 82755A13) between the magnets, attach one string to a fixed support and the other string over a low-friction pulley, attached to a small bucket. Weights are added to the bucket until the magnets separate. A schematic is shown as an inset to Fig. 7. The weight required to separate is equal to the magnetic strength at this separation distance. This experiment was run with two 6mm E52100 Alloy steel spheres in a 3T Siemens Skyra MRI scanner, resulting in remarkable similarity to the model (5), as shown in Fig. 7.

Neodymium magnets come in a variety of grades. Using the same plastic feeler gauge setup, using 5mm diameter neodymium beads (<http://neocubes.com>), provided 43% the force of equivalent magnetically saturated E52100 steel spheres. According to tests of 16 N42 neodymium spherical magnets¹, N42 magnets have 77% the magnetic saturation of E52100 steel spheres in a 3T MRI.

Because most MRI scanners can apply forces 36-71% the force due to gravity, it is necessary to offset the force of gravity using buoyancy forces. Ideally the Gauss gun

¹<https://www.kjmagnetics.com/magnetsummary.asp>

components would be neutrally buoyant

$$\rho_{\text{H}_2\text{O}} \sum v_i = \sum \rho_i v_i. \quad (12)$$

Early prototypes used small hollow compartments to float the Gauss gun components at the water surface, as shown in Fig. 9. A list of materials used for Gauss gun prototypes is given in Table I. The shells are printed using a Stratasys Objet printer with VeroWhite polymer, which is only slightly more dense than water. The E52100 alloy steel spheres are largest weight contributors to the Gauss gun. The separator material must have low magnetic saturation and transmit kinetic energy by having a high coefficient of restitution. Aluminum, tungsten, and titanium are all reasonable replacements, but tungsten is heavy, and aluminum is soft. The separator need not be the same diameter as the spheres and instead can be a thin rod, further lowering the weight.

TABLE I
MATERIAL PROPERTIES FOR GAUSS GUN

material	density g/cm ³	permeability H/m	Mod of elasticity GPa
VeroWhite	1.17	—	2.6-3.0
E52100 steel	7.81	1.3×10^{-4}	210
aluminum	2.70	1.3×10^{-6}	68.0
tungsten	19.3	3.3×10^{-7}	400
titanium	4.50	1.6×10^{-6}	116

IV. EXPERIMENTS

The MRI Gauss gun components described in Section III, and shown in Figs. 5 and 6, were tested in a Siemen's Skyra 3T clinical MRI scanner. Experiments tested penetration depth as a function of needle size and the ability of components to self-assemble.

A. Penetration Tests

Several experiments were conducted to test the ability of the MRI-Gauss gun at tissue penetration. The tests use a brain model composed of a solidified 0.5% agarose gel solution [18]. A 30mm block of agarose was used and placed near the isocenter of a Siemen's Skyra 3T MRI scanner. The delivery component, loaded with either an 18, 20, or 26-gauge needle was placed against the solution. Zero, one, or two barrel components were attached, and the trigger component was then manually pushed toward the assembled Gauss gun. Needle penetration was measured using a plastic ruler mounted underneath the transparent agar solution.

The experiment results are represented in Fig. 8. Five trials were recorded for each needle size. The penetration distance increases as the gauge increases (needle diameter decreases).

B. Self-Assembly Tests

Figure 10 shows photos from two experiments with Gauss gun assembly and membrane penetration. The experiments were performed under MRI control, using gradients in the x and z direction of $\pm 23\text{mT/m}$. The workspace was a plastic toolbox (McMaster-Car 8704T73) filled with water. The Gauss gun components were mounted on floats and colored

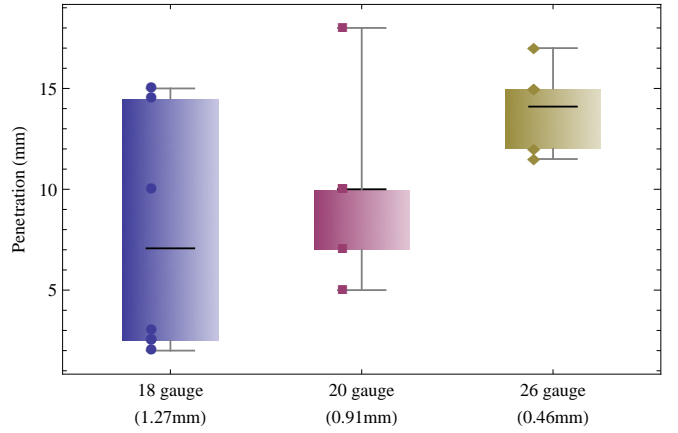


Fig. 8. Penetration of the three needle tips with 1mm sphere shown in Fig. 5 into 5% agar solution, using single-stage MRI Gauss gun.

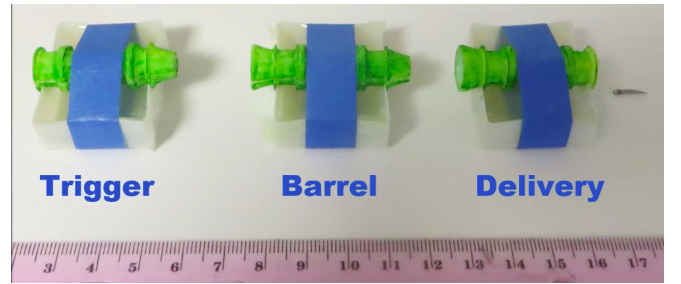


Fig. 9. Gauss gun components used in MRI experiments

green to increase visibility. Three tests were performed, and are included in the video attachment. The first two experiments each used a *delivery* and a *trigger* component and fired 18-gauge needle tips welded to 1mm spheres into a membrane model, a water balloon filled with blue dye. The third experiment tested ranged delivery, by firing the needle projectile using a *delivery*, *barrel*, and *trigger* component to penetrate a membrane model from a distance of 240 mm.

C. MRI Tracking

The MRI could provide an integrated environment for intervention using the Gauss gun. Pre-operative and post-operative images could be acquired with the MRI as depicted in Fig. 11, showing the membrane model before and after Gauss gun deployment, assembly, and firing. The individual components of the Gauss gun could also be tracked in real-time using RF-selective excitation [19]. Distinct peaks, corresponding to the locations of the Gauss gun components, can be acquired in less than 20ms, as shown in Fig. 12.

V. CONCLUSION

This paper presented a model, verification, and optimizations for multi-stage Gauss guns. The traditional Gauss gun depends on permanent magnets and steel spheres. To use stored magnetic potential energy, a new MRI Gauss gun was designed. The MRI Gauss gun can be self-assembled into a larger tool to increase puncture force, far stronger than the forces possible with MRI gradients. Experiments performed using a clinical MRI scanner illustrate the potential of this device. Future work should investigate how the design can be

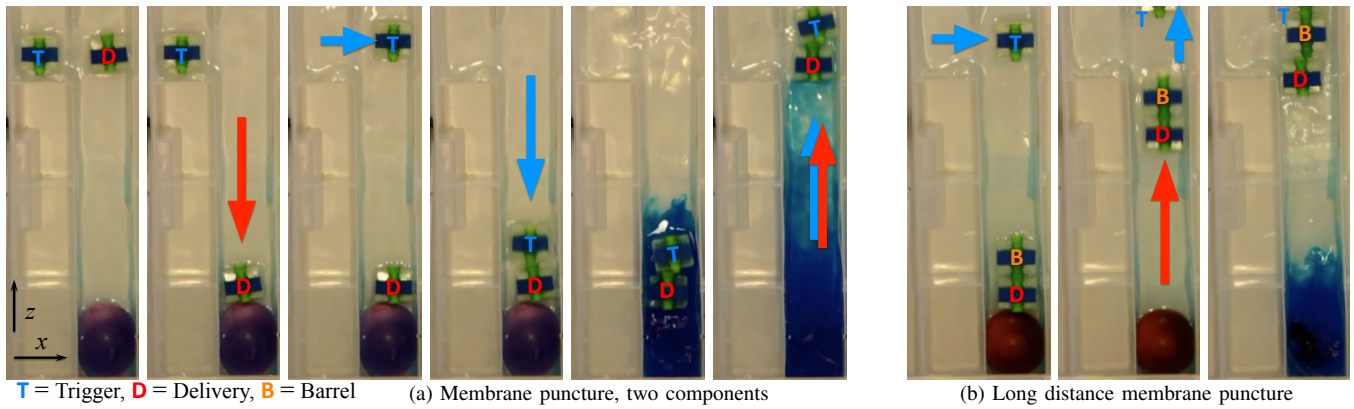


Fig. 10. Photos from an experiment within the MRI bore. The membrane model is a water balloon filled with dye. See the video attachment.

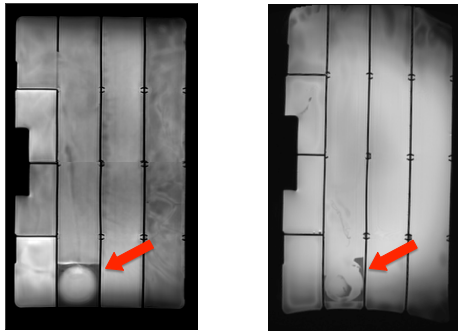


Fig. 11. A T2 weighted Turbo Spin Echo MRI image showing the dye-filled balloon before and after penetration. The agar used to stabilize the balloon is visible in both images.

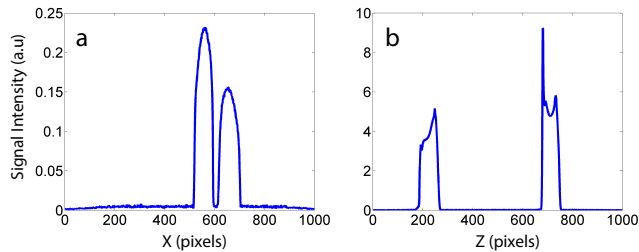


Fig. 12. MRI projections of the Gauss gun components using a custom MR sequence based on a spin echo acquisition with a pixel size of 0.59mm. (a) Projection along the x -axis corresponding to the Gauss gun components in Fig. 10a, frame 2. (b) Projection along the z -axis corresponding to the Gauss gun components in Fig. 10a, frame 3.

optimized for clinical use cases and implement closed-loop control of the components.

REFERENCES

- [1] R. C. Ritter, M. S. Grady, M. A. H. III, and G. T. Gillies, *Computer-integrated Surgery: Technology and Clinical Applications*. The MIT Press, 1996, ch. 26 Magnetic Stereotaxis: Computer-Assisted, Image-Guided Remote Movement of Implants in the Brain, pp. 363–370.
- [2] K. Ishiyama, M. Sendoh, A. Yamazaki, and K. Arai, “Swimming micro-machine driven by magnetic torque,” *Sensors and Actuators A: Physical*, vol. 91, no. 1, pp. 141–144, 2001.
- [3] A. Chanu, O. Felfoul, G. Beaudoin, and S. Martel, “Adapting the clinical MRI software environment for real-time navigation of an endovascular untethered ferromagnetic bead for future endovascular interventions,” *Magn Reson Med*, vol. 59, no. 6, pp. 1287–1297, Jun. 2008.
- [4] P. Vartholomeos, M. Akhavan-Sharif, and P. E. Dupont, “Motion planning for multiple millimeter-scale magnetic capsules in a fluid environment,” in *IEEE Int. Conf. Rob. Aut.*, May 2012, pp. 1927–1932.
- [5] P. Vartholomeos, C. Bergeles, L. Qin, and P. E. Dupont, “An MRI-powered and controlled actuator technology for tetherless robotic interventions,” *Int. J. Rob. Res.*, vol. 32, no. 13, pp. 1536–1552, 2013.
- [6] A. Becker, O. Felfoul, and P. E. Dupont, “Simultaneously powering and controlling many actuators with a clinical MRI scanner,” in *IEEE/RJS International Conference on Intelligent Robots and Systems (IROS)*, 2014, pp. 2017–2023.
- [7] A. Eqtami, O. Felfoul, and P. E. D. E. Dupont, “MRI-powered closed-loop control for multiple magnetic capsules,” in *IEEE/RSJ Int. Conf. Intelligent Robots and Systems*, 2014, pp. 3536–3544.
- [8] A. Bigot, C. Tremblay, G. Soulez, and S. Martel, “Magnetic resonance navigation of a bead inside a three-bifurcation pmma phantom using an imaging gradient coil insert,” *Robotics, IEEE Transactions on*, vol. 30, no. 3, pp. 719–727, June 2014.
- [9] W. K. Cho, J. A. Ankrum, D. Guo, S. A. Chester, S. Y. Yang, A. Kashyap, G. A. Campbell, R. J. Wood, R. K. Rijal, R. Karnik, R. Langer, and J. M. Karp, “Microstructured barbs on the north american porcupine quill enable easy tissue penetration and difficult removal,” *Proceedings of the National Academy of Sciences*, vol. 109, no. 52, pp. 21 289–21 294, 2012. [Online]. Available: <http://www.pnas.org/content/109/52/21289.abstract>
- [10] O. Felfoul, A. Becker, C. Bergeles, and P. E. Dupont, “Achieving commutation control of an MRI-powered robot actuator,” *IEEE Trans. on Robotics*, vol. under review, 2014.
- [11] M. Mahvash and P. Dupont, “Mechanics of dynamic needle insertion into a biological material,” *Biomedical Engineering, IEEE Transactions on*, vol. 57, no. 4, pp. 934–943, April 2010.
- [12] J. A. Rabchuk, “The gauss rifle and magnetic energy,” *The Physics Teacher*, vol. 41, no. 3, pp. 158–161, 2003.
- [13] D. Kagan, “Energy and momentum in the gauss accelerator,” *The Physics Teacher*, vol. 42, no. 1, pp. 24–26, 2004.
- [14] R. Schill, “General relation for the vector magnetic field of a circular current loop: a closer look,” *Magnetics, IEEE Transactions on*, vol. 39, no. 2, pp. 961–967, Mar 2003.
- [15] A. T. Becker, “Optimizing a Gauss Gun, Wolfram Demonstrations Project,” Oct. 2014. [Online]. Available: <http://demonstrations.wolfram.com/OptimizingAGaussGun/>
- [16] C. for Disease Control, Prevention *et al.*, “Gastrointestinal injuries from magnet ingestion in children—united states, 2003–2006,” *MMWR: Morbidity and Mortality Weekly Report*, vol. 55, no. 48, pp. 1296–1300, 2006.
- [17] M. F. Kircher, S. Milla, and M. J. Callahan, “Ingestion of magnetic foreign bodies causing multiple bowel perforations,” *Pediatric radiology*, vol. 37, no. 9, pp. 933–936, 2007.
- [18] I. Howard, M. A. B. Abkes, M. Ollendieck, M. Noh, R. C. Ritter, and G. Gillies, “Measurement of the force required to move a neurosurgical probe through in vivo human brain tissue,” *Biomedical Engineering, IEEE Transactions on*, vol. 46, no. 7, pp. 891–894, July 1999.
- [19] O. Felfoul, J.-B. Mathieu, G. Beaudoin, and S. Martel, “In vivo mr-tracking based on magnetic signature selective excitation,” *Medical Imaging, IEEE Transactions on*, vol. 27, no. 1, pp. 28–35, 2008.